Electronic Supplementary Material (ESI) for Journal of Materials Chemistry C.

Supplementary Information

In-situ **photogenerated hydroxyl radicals in the reaction atmosphere for the accelerated crystallization of solution-processed functional metal oxide thin films**

Alicia Gómez-López[+], Y.Andrea Rivas, Sergio López-Fajardo, Ricardo Jiménez, Jesús Ricote, Carlos Pecharromán, Isabel Montero, Iñigo Bretos, M.Lourdes Calzada**

Instituto de Ciencia de Materiales de Madrid, Consejo Superior de Investigaciones Científicas (ICMM-CSIC). C/ Sor Juana Inés de la Cruz, 3. Cantoblanco. 28049 – Madrid (Spain)

[+] Present address: Instituto de Catálisis y Petreoquímica (ICP-CSIC). C/ Marie Curie, 2. Cantoblanco. 28049 – Madrid (Spain)

*Corresponding authors: ibretos@icmm.csic.es, lcalzada@icmm.csic.es

Table S1. Summary of high-*k* dielectric films, amorphous and crystalline (ferroelectrics), prepared by solution deposition methods at temperatures ≤ 400 °C. The electrical properties of these films are collected in this table to show their potential for using in functional electronic devices.

Amorphous dielectric oxide films	Processing temperature (℃)	Film thickness (nm)	Delectric constant (*k*)	Breakdown field (MV/cm)	Reference
$AlPO_x$	350	148-185	4.8	~ 10	[1]
$HfSO_x$, $ZrSO_x$	325	150-300	9-12	~ 6	[2]
$AlPO_x$	350	180	5.2	~ 5	[3]
ZrO_x	300	149	10	---	[4]
HfO_x	400	120	13	~ 5.5	[5]
$Zr/Al/ZrO_x$	350	250	14.8	~ 3.4	[6]
$ZrAlO_x$	350	100	11.8	~ 8	[7]
AlOx	350	242	144	~ 4	[8]
ZrO_x	350	210	14.8	~ 2.8	[9]
$ZrOx/AlO_x/ZnO_x$	350	250	46	~ 3.4	[10]
$TiO_2 - AlPO_x$	350	150	8	~ 5.4	[11]
Gd_2O_3	400	100	10-12	~ 3.5	[12]
ZrO_x	450	100	19.1	~ 3.2	[13]
ZrO_x	350	210	14.8	~ 2.8	[8]
AlO_x	100	151	157	---	[14]
HfO_x	200	60	10.23	~ 6	[15]
La_2O_3-Al_2O_3 flexible	350	100	10.72	~ 4.8	[16]
Ferroelectric crystalline oxide films	**Processing temperature (℃)**	**Film thickness (nm)**	**Delectric constant (*k*)**	**Remanent polarization ($\mu C/cm^{-2}$)**	**Reference**
$(Pb_{0.925}La_{0.05}Zr_{0.30}Ti_{0.7}O_3)$	400	250	450	~ 12.5	[17]
$Pb_0Zr_{0.30}Ti_{0.7}O_3$	400	250	190	~ 22	[18]
$Pb_{0.76}Ca_{0.24}TiO_3$	400	200	180-300	~ 14	[19]
$PbTiO_3$	400	200	---	~ 12	[20]
$(Bi_{0.5}Na_{0.5})_{0.945}Ba_{0.055}TiO_3$	400	200	---	~ 8	[21]
$Pb_0Zr_{0.30}Ti_{0.7}O_3$ flexible	350	200	100	~ 18	[22]
$Bi_{1.5}Zn_{0.9}Nb_{1.35}Ta_{0.15}O_{6.9}$	350	110	50	~ 2.5	[23]
$BiFeO_3$ flexible	300	100	---	~ 2.8	[24]
$BiFeO_3$; $Pb_0Zr_{0.30}Ti_{0.7}O_3$ flexible	350	180	80	5.5-10	[25-27]
$Pb_{1.2}Zr_{0.48}Ti_{0.52}O_3$	400	150	480	~ 25	[28]
$Pb_{1.2}Zr_{0.48}Ti_{0.52}O_3$ rigid and flexible	350	225	190	~ 14	this work
$BiFeO_3$ rigid and flexible	350	140	140	~ 9	this work

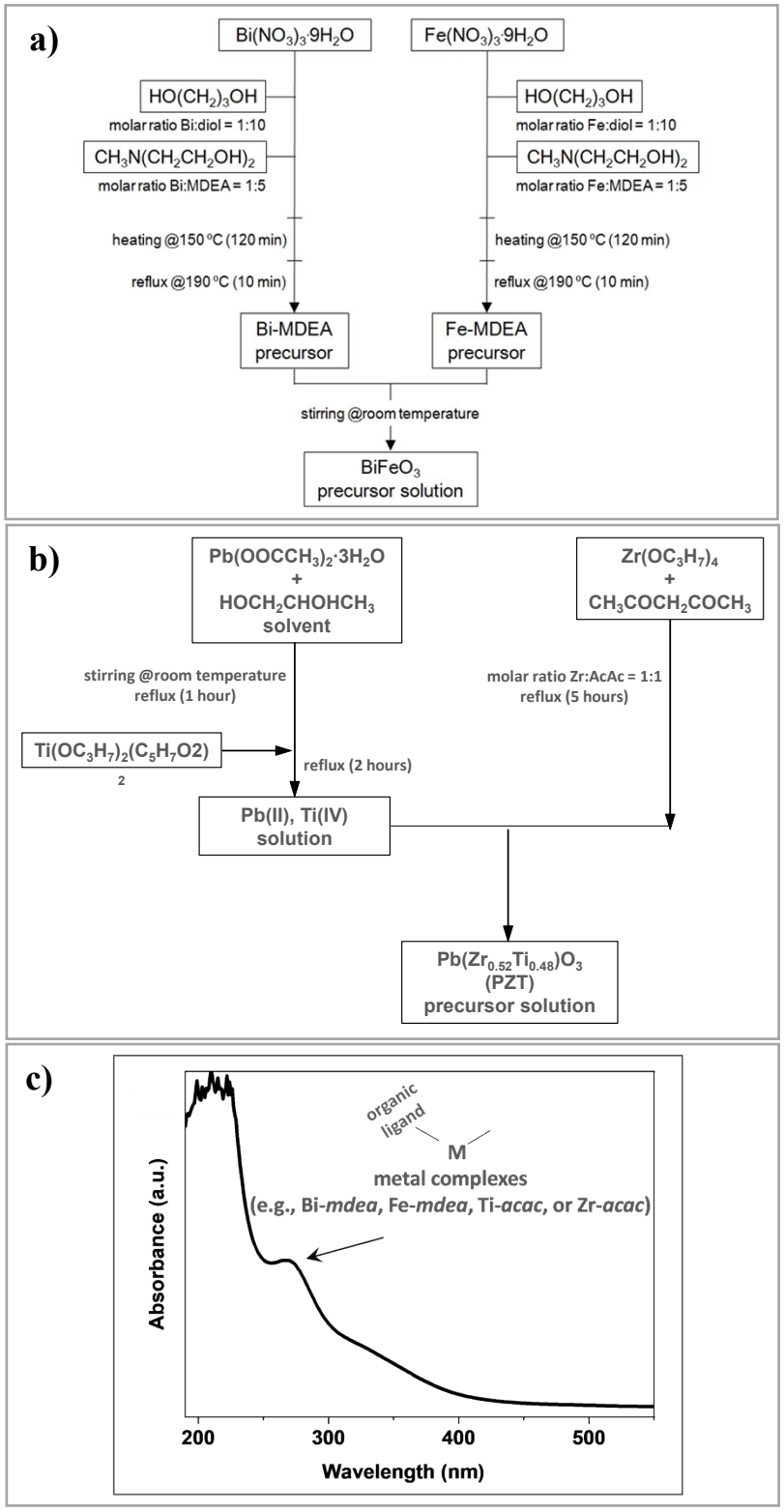

Figure S1. Synthesis schemes of the a) $BiFeO_3$ and b) $Pb(Zr_{0.30}Ti_{0.70})O_3$ (PZT) precursor solutions that have been tested in this work.[29-31] Binary oxide films like Bi_2O_3 were prepared from the intermediate solutions synthesized for the single cation. These particular solutions are photosensitive, since molecular metal complexes with high absorption in the UV range have been synthesized or used as reagents during the preparation of the precursor solutions. c) Representative UV-Vis spectra of the $BiFeO_3$ and PZT precursor solutions, which have been adapted with permission[19,21] Wiley-VCH Verlag GMBH and Royal Society of Chemistry

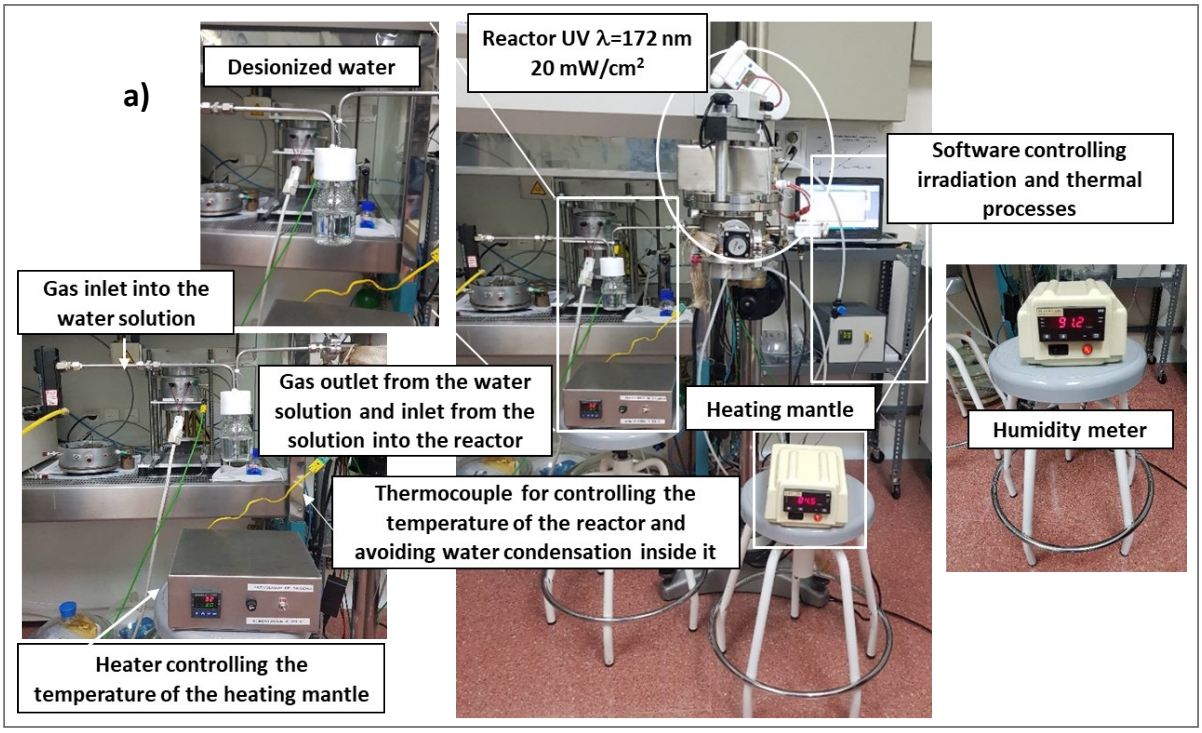

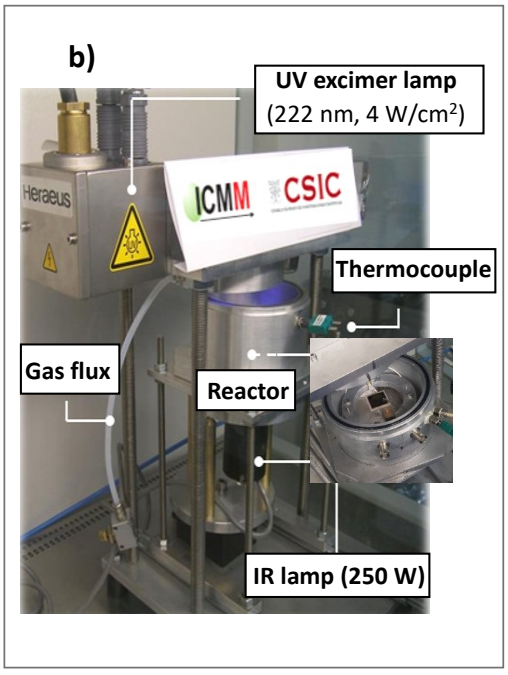

Figure S2. Laboratory-scale UV-irradiation reactors used for the processing of the films.
a) Reactor with a high-intensity excimer lamp of λ=172 nm. In this reactor, free hydroxyl radicals (•OH) are generated *in-situ* in the UV-irradiation atmosphere. For the generation of the •OH radicals, a saturated water (H_2O) vapor is introduced in the irradiation chamber after passing pure oxygen (O_2) gas through deionized water.[31] b) Reactor with a high-intensity excimer lamp of λ=222 nm. In this reactor, ozone (O_3) is generated in the UV-irradiation atmosphere by introducing pure oxygen (O_2) in the irradiation chamber. Both UV-reactors use commercial hot-plate ceramic heaters (ULTRAMIC Advanced Ceramic Heaters) for the heating of the films (between 150ºC and 250ºC) during the UV-irradiation processes.[22]

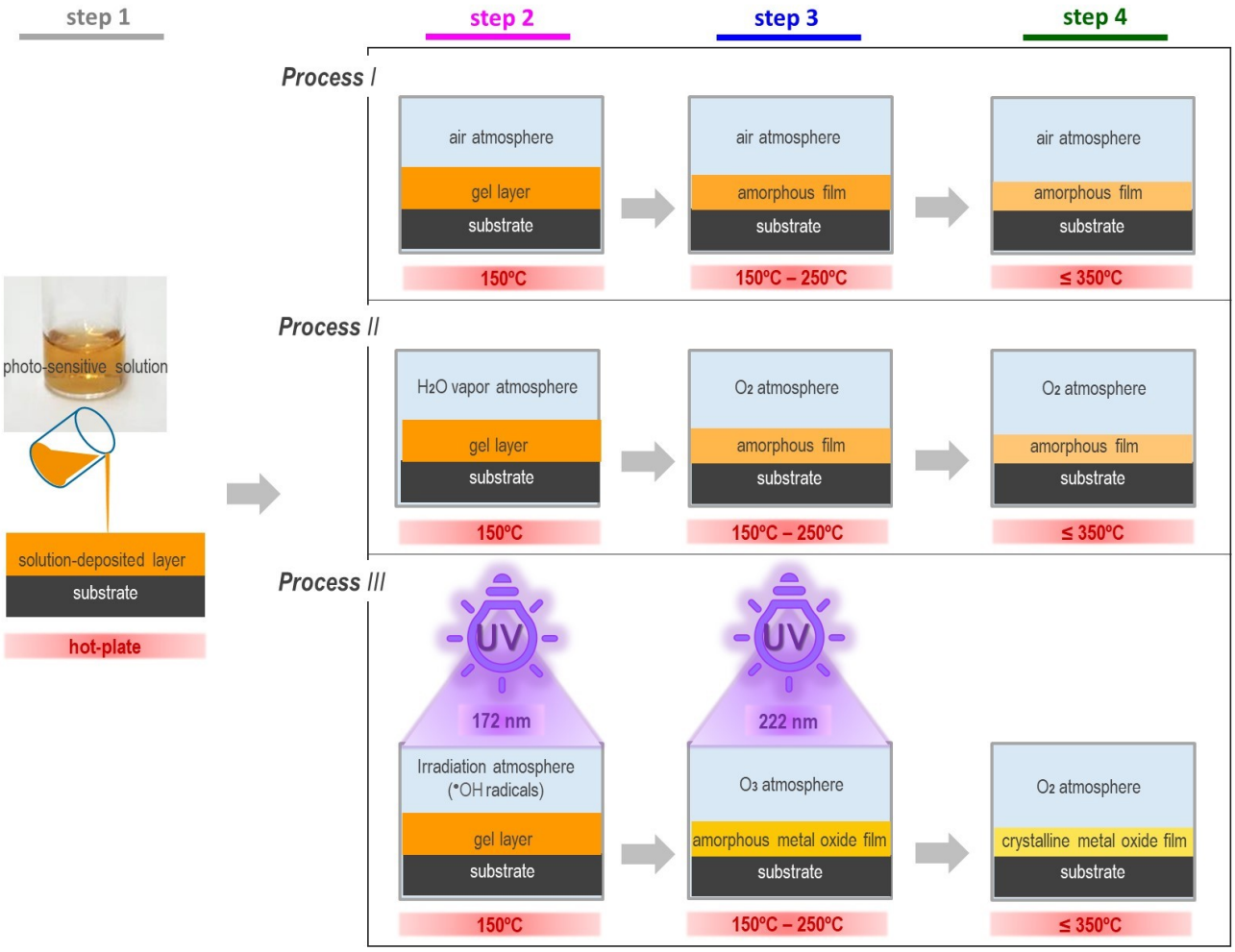

Figure S3. Process III corresponds to the hydroxyl free radicals method developed in this work for accelerating the formation and crystallization of solution-processed functional metal oxide thin films. This processing method includes different steps: solution deposition (step 1), UV-irradiation of the deposited layer in •OH and O_3 atmospheres (steps 2 and 3, respectively), and low-temperature heating for the film crystallization (step 4). The Process I and II shown in the figure are those carried out in the same way as Process III, but without UV-irradiation, under the water vapor and O_2 atmosphere used in the steps 2 and 3, respectively, for the *in-situ* generation of •OH free radicals and O_3 atmospheres (Process II), and in conventional air atmosphere (Process I).

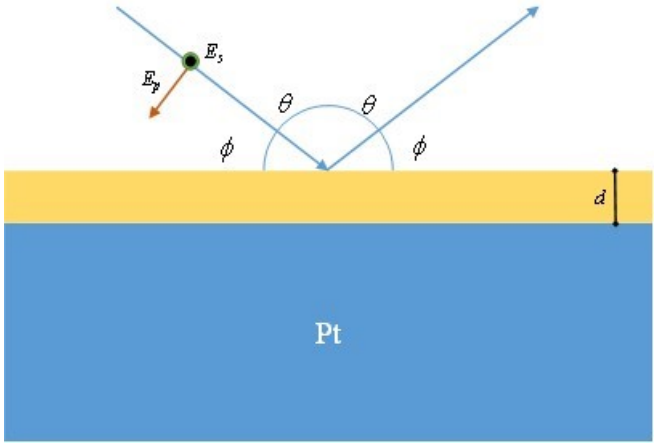

Figure S4. Scheme of the configuration used for the study by IRRAS of the films of this work that are deposited on Pt-coated Si(100) substrates. The incident angle used here is very close to 90º, *d* is the film thickness (below 100 nm), E_p and E_s are the perpendicular and parallel polarization, respectively.

Infrared spectroscopy is especially suited to the herewith employed samples as it is sensitive to the dipolar moment, which is present both at the organic groups of the precursors and intermediate products, as well as to amorphous and crystalline perovskite solids. The simultaneous requirement to characterize both, organic and inorganic compounds, requires to cover a very broad IR spectral range (from 200 to 4000 cm^{-1}). Due to the small thickness of the film on a Pt substrate, as well as the IR absorbing character of the employed substrates, we have considered that the most adequate FTIR technique for studying these samples is Infrared Reflection Absorption Spectroscopy (IRRAS).[32] This technique is very sensitive to thin layers over metallic substrates, but requires the use of polarizers and a grazing angle (80º in this case). Figure S4 shows a scheme of the configuration of the IRRAS technique used for the characterization of the films of this work. The films studied here by IRRAS have a thickness below 100 nm and are deposited on Pt-coated Si(100) substrates.
In our case, we take the ratio between the parallel and the perpendicular polarization. Using the transfer matrix procedure[33] and after some algebra, assuming that the layer thickness is much smaller than the wavelength, the refractive index of the metallic substrate is much larger than that of the layer, and that the incident angle is very close to 90º, it can be shown that the ratio between polarizer ρ, is given by:

$$\rho \cong -1 - i\mu\left(1 - \frac{1}{n^2}\right)$$

$$\mu = \frac{4\pi d\omega}{\phi}$$

Where *d* is the layer thickness, *w* the wavenumber, *f*=p/2-*q* the value of grazing angle (being *q* the incident angle), and *n* the refractive index of the layer. If we consider the region of lattice vibrations, the refractive index of the layer is considerably large, so that it is given by a harmonic oscillator model[34]

$$n^2 = \varepsilon_r = \varepsilon_\infty \frac{\omega_L^2 - \omega^2 - i\gamma_L\omega}{\omega_T^2 - \omega^2 - i\gamma_T\omega}$$

Where w_L and w_T are the longitudinal and transversal phonon frequencies, and g_T and g_L their damping constant. So that

$$\rho \cong -1 - i\mu\left(1 - \varepsilon_\infty \frac{\omega_T^2 - \omega^2 - i\gamma_T\omega}{\omega_L^2 - \omega^2 - i\gamma_L\omega}\right)$$

It is very easy to figure it out that minima of this expression will be very close to w_L, that is, we are going to measure the longitudinal frequencies of the optical phonons. On the other hand, in case of an organic IR mode, the refractive index can be approximated as: $n \cong n_0 + i\alpha$, being $\alpha \ll n_0$. Because the experimental magnitude taken by IRRAS is $|r|^2$, in case of weekly absorbing modes we get:

$$|\rho|^2 = 1 + \left(\frac{n_0^2 - 1}{n_0^2}\right)^2 \mu^2 - \frac{4\mu}{n_0^3}\alpha$$

In this case, the spectrum is a line close to 1 minus a quantity proportional to the absorption term of the refractive index. As in these substances, the transverse-longitudinal phonon splitting is very weak, minima at very similar positions as conventional absorption measurements will be taken.

The use of conventional X-ray Photoelectron Spectroscopy (XPS) typically involves the surface cleaning and depth profile with Ar ions. Ion beam bombardment induces different types of damage, including change in chemical bond state, preferential sputtering, compound decomposition, and surface roughness. In the case of the very thin $BiFeO_3$ films studied here, such damage can be avoided by the use of Angle Resolved X-ray Photoelectron Spectroscopy (ARXPS) (Figure S5a).

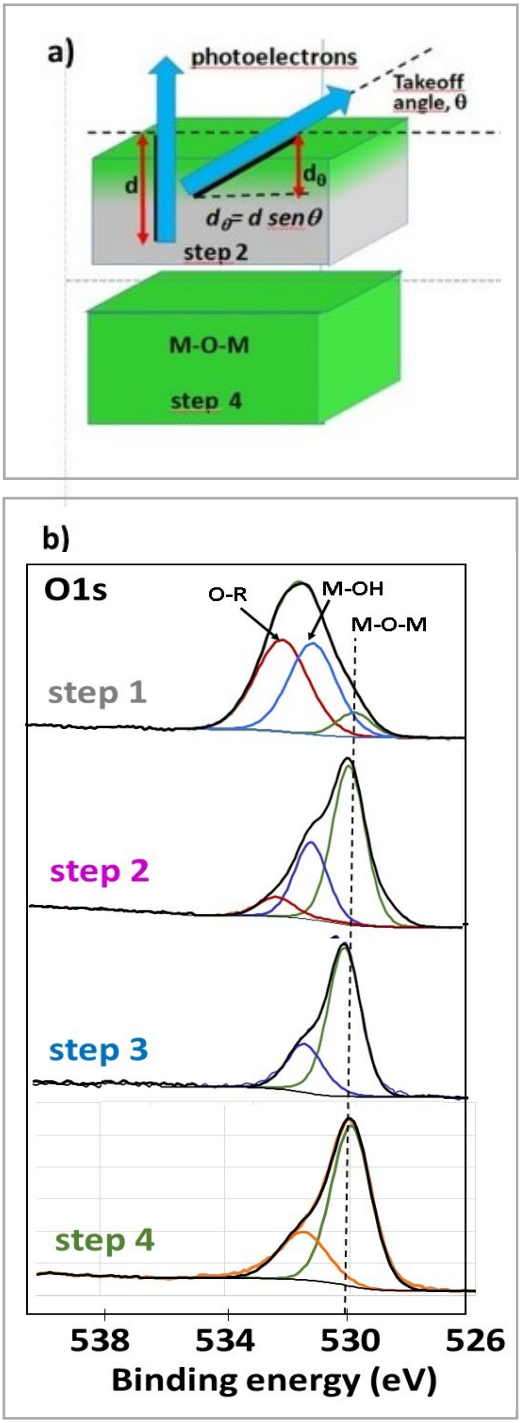

Figure S5. a) Scheme of the Angle-Resolved X-ray Photoemission Spectroscopy (ARXPS) used for the characterization of the films. A Mg Kα X-ray source (hv = 1253.6 eV), an analyzer with a pass energy of 20 eV and a micrometric manipulator, XYZθ, for sample positioning and tilting have been used. The ARXPS analyses were performed with *take-off* angles of 40° and 90° with respect to the hemispherical analyzer. In this way, at 40° the analyzed photoelectrons come from the region closest to the surface (up to 10 nm depth) and their signal can be compared with that of the photoelectrons resulting from the typical analysis at 90°. ARXPS is a non-destructive technique that does not lead to the modifications produced in the samples when conventional argon ion bombardment is used to obtain the depth profiles of the samples. This technique is available at the ICMM-CSIC, under the supervision of Prof. Montero.
b) O1s core level ARXPS spectra for the samples after the steps 1 to 4 of the process. Experimental data here shown were acquired with a normal configuration using a tilt angle of 90º. A Shirley background was used.
Step 1: Three components of the O1s spectrum were decomposed from an experimental peak with a FWHM of ~3.3 eV. These components are called peaks I, II and III, from low to high binding energies. They are associated to oxygen in oxides (M – O – M compounds) (~530,1 eV), in hydroxides ($M(O–H)_x$) (~531,8 eV) and in organic compounds (O – R) (~533,1 eV), respectively.

Step 2: A noticeable shift of the O1s spectrum to lower binding energies is observed, recording an experimental peak where the FWHM has been reduced to ~1.6 eV. This O1s experimental peak can also be decomposed in three different components, also identified as peak I, II and III. *Step 3*: the experimental O1s peak has the same FWHM of 1.6 eV as in the

Step 2, but now the relative intensity has decreased by a factor of 2. This spectrum can be fitted only to two peaks, I and II. *Step 4*: An experimental O1s spectrum is obtained that can also be decomposed in two peaks, I and II. The position of the peak I has now the characteristic binding energy of oxygen in oxides, but probably with a more ordered structure (crystallinity) and with a binding energy that corresponds to that of transition metal oxides in M-O-M compounds, ~530.1 eV. The peak II is also associated to transition metal oxides. It appears as a shoulder of the main peak because it indicates the participation in the oxide of different transition metal cations. This results in metal-oxygen bonds with different binding energies, in this case Bi – O and Fe – O. Similar O1s spectra have been reported in the literature, which have been associated to transition complex metal oxides.[35,36]

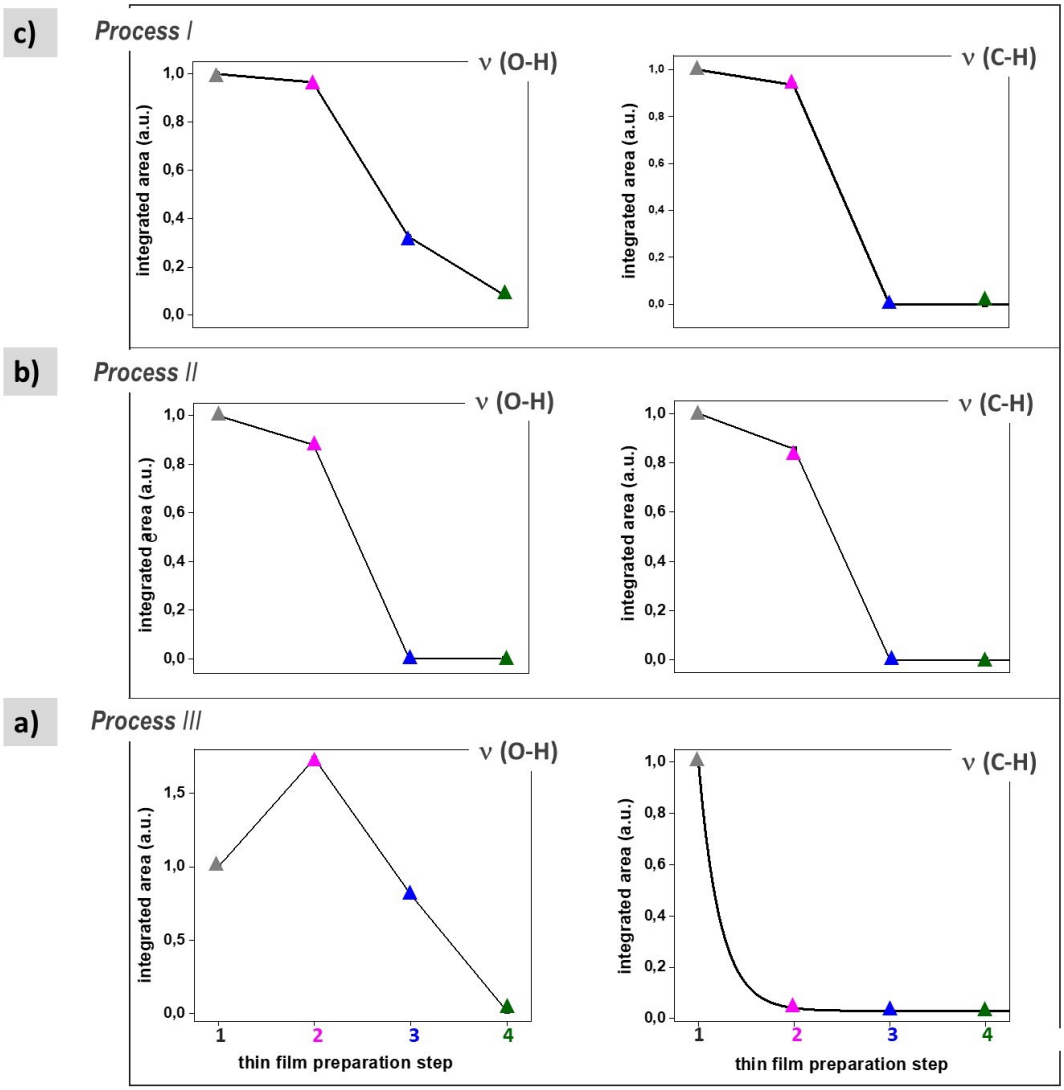

Figure S6. Integrated areas of the ν(O – H) and ν(C – H) FTIR bands calculated for the films after subjecting them to the different steps of the processing method following the Processes I, II and III, a), b) and c), respectively, described in Figure S3.

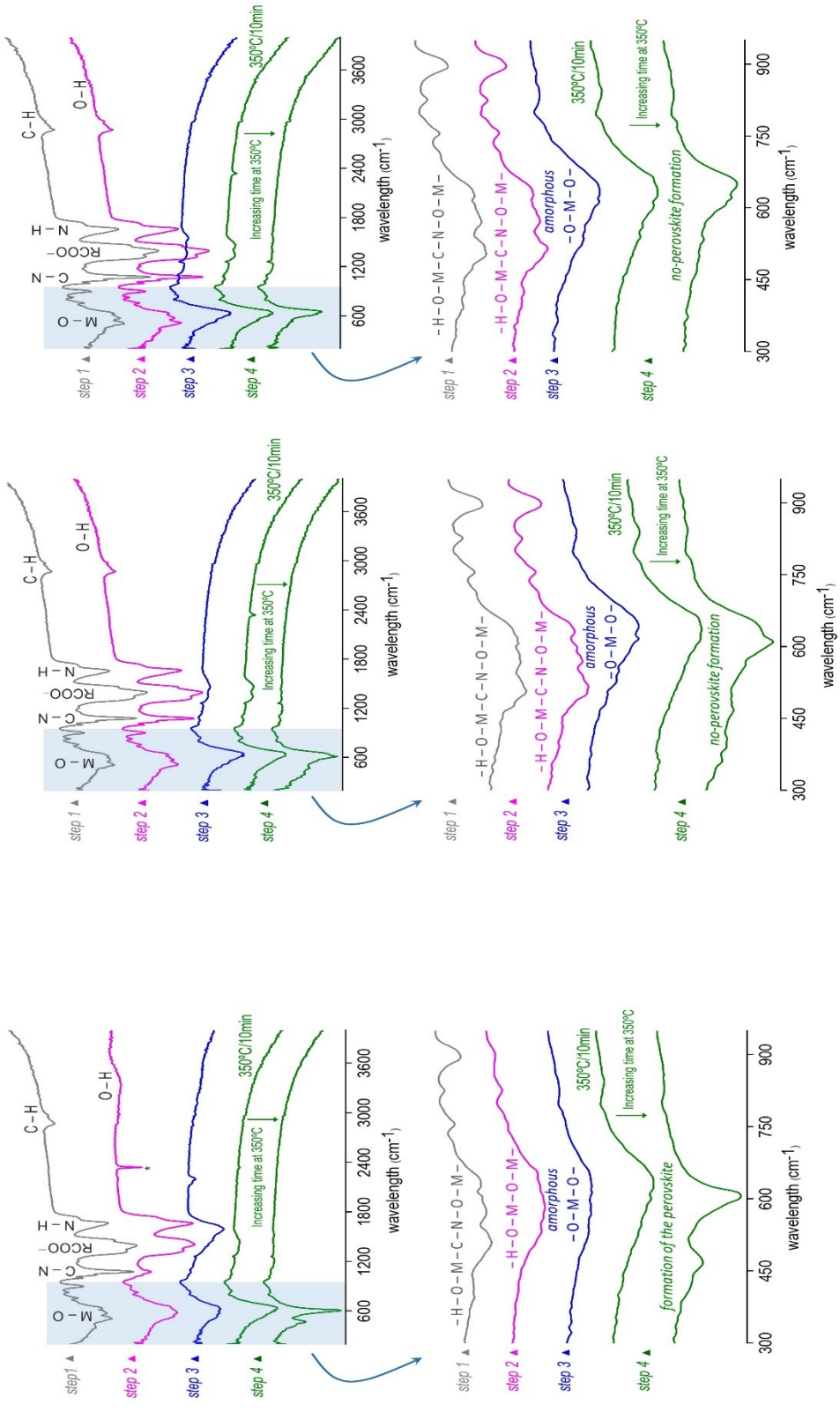

Figure S7. Infrared Reflection Absorption Spectroscopy (IRRAS) spectra between 200 cm^{-1} and 4000 cm^{-1}, and in the region of the M – O bonds (below 800 cm^{-1}) recorded for the films obtained after the different steps of the Processes I, II and III described in Figure S1. These measurements were carried out on films deposited on $Pt/TiO_2/SiO_2/(100)Si$.

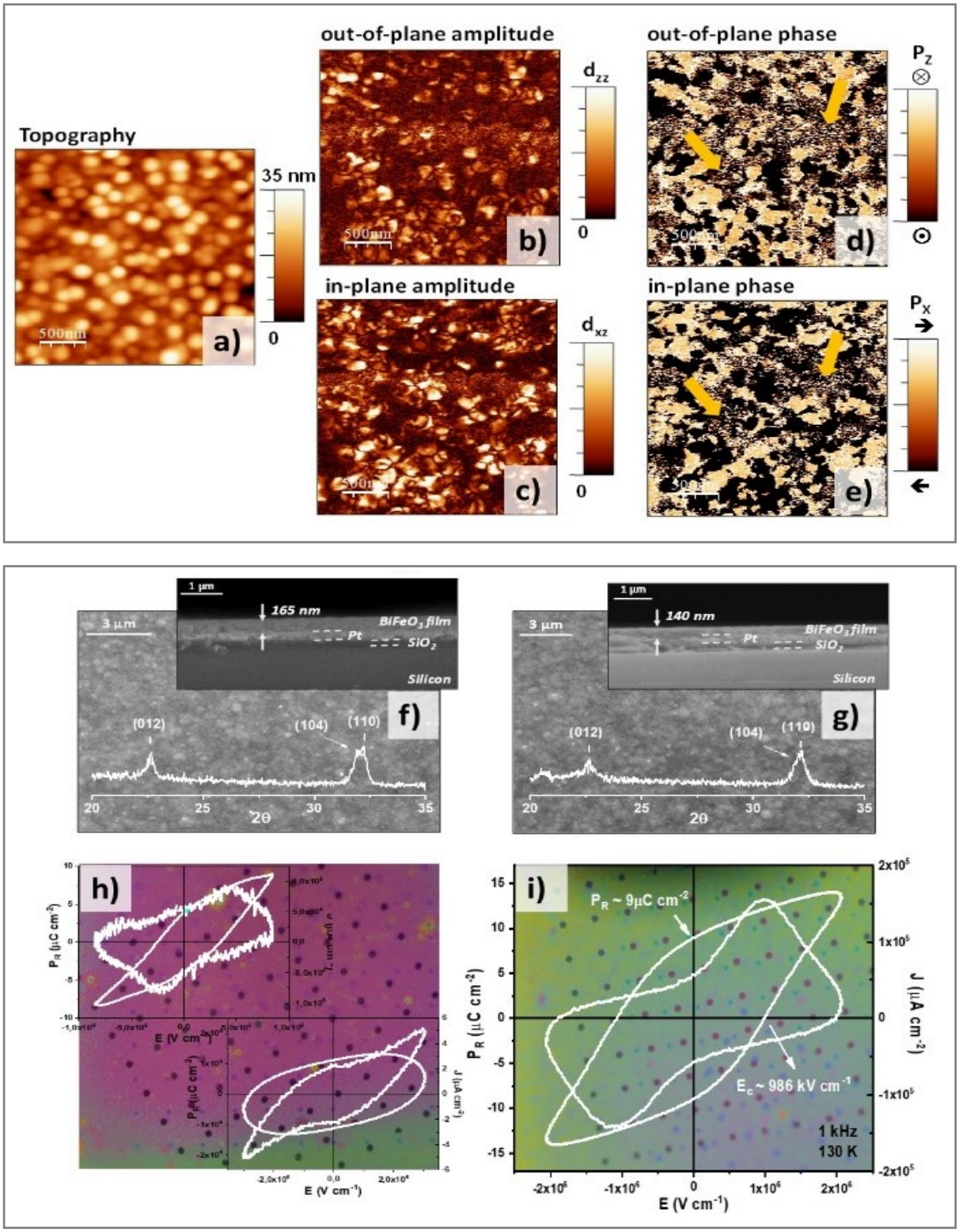

Figure S8. a) Topography, b), c) out-of-plane and d), e) in-plane amplitude and phase images of the $BiFeO_3$ perovskite thin films obtained after both UV-irradiation steps (step 2 in $^{\bullet}OH$ atmosphere and step 3 in O_3 atmosphere), and after a thermal treatment at 350 ºC. The films show a clear piezoelectric response. Areas with poor contrast, indicated with yellow arrows in the phase images, correspond to regions of the films with incipient crystallization. f), g) Plan-view and cross-section FEGSEM images, and X-ray diffraction patterns of the $BiFeO_3$ thin

films prepared on Pt-coated silicon substrates without applying the step 3 and with the complete devised processing method, respectively. The reflections of the $BiFeO_3$ perovskite have been indexed with the JCPDS-ICDD card No. 01-86-1518. h), i) Photographs of the array of the capacitors fabricated for the electrical characterization and ferroelectric hysteresis loops measured in the former films. Note that the film thickness of the films to which the step 3 was not applied is larger (~165 nm) than that of the film subjected to the complete process, including this UV-irradiation in the step 3 (~140 nm). The former is around a 18% thicker than the latter. This is associated to a lack of densification because residual amorphous phases, organic residuals or pores have not been totally eliminated from the former film. As a result, many of the capacitors fabricated in this film are short-circuited, and the ferroelectric hysteresis loops of those capacitors that have been able to be measured, show a large amount of non-switching contributions (leakage currents and conduction). On the contrary, well-defined ferroelectric hysteresis loops are obtained in the other film, where around a 95% of the capacitors have high permittivities and low dielectric losses. This is because this second UV-irradiation at λ=222 nm in an O_2 atmosphere (which results under irradiation at this wavelength in a strong O_3 oxidizing atmosphere) not only increases the film densification as detected by the difference in thickness of the films shown in f) and g), but also this UV-treatment produces the elimination of defects (porosity, carbonaceous residuals, oxygen vacancies, etc.), which decreases the non-switching contributions (*i.e.*, leakage currents and conduction), improving the ferroelectric response of the film as observed from the comparison of the ferroelectric hysteresis loops of h) and i). This is in accordance with previous results reported in the literature in which UV-light treatments are used as conditioning treatments for just improving the electrical response of crystalline ferroelectric films and thin film transistors processed at high temperatures.[37-39]

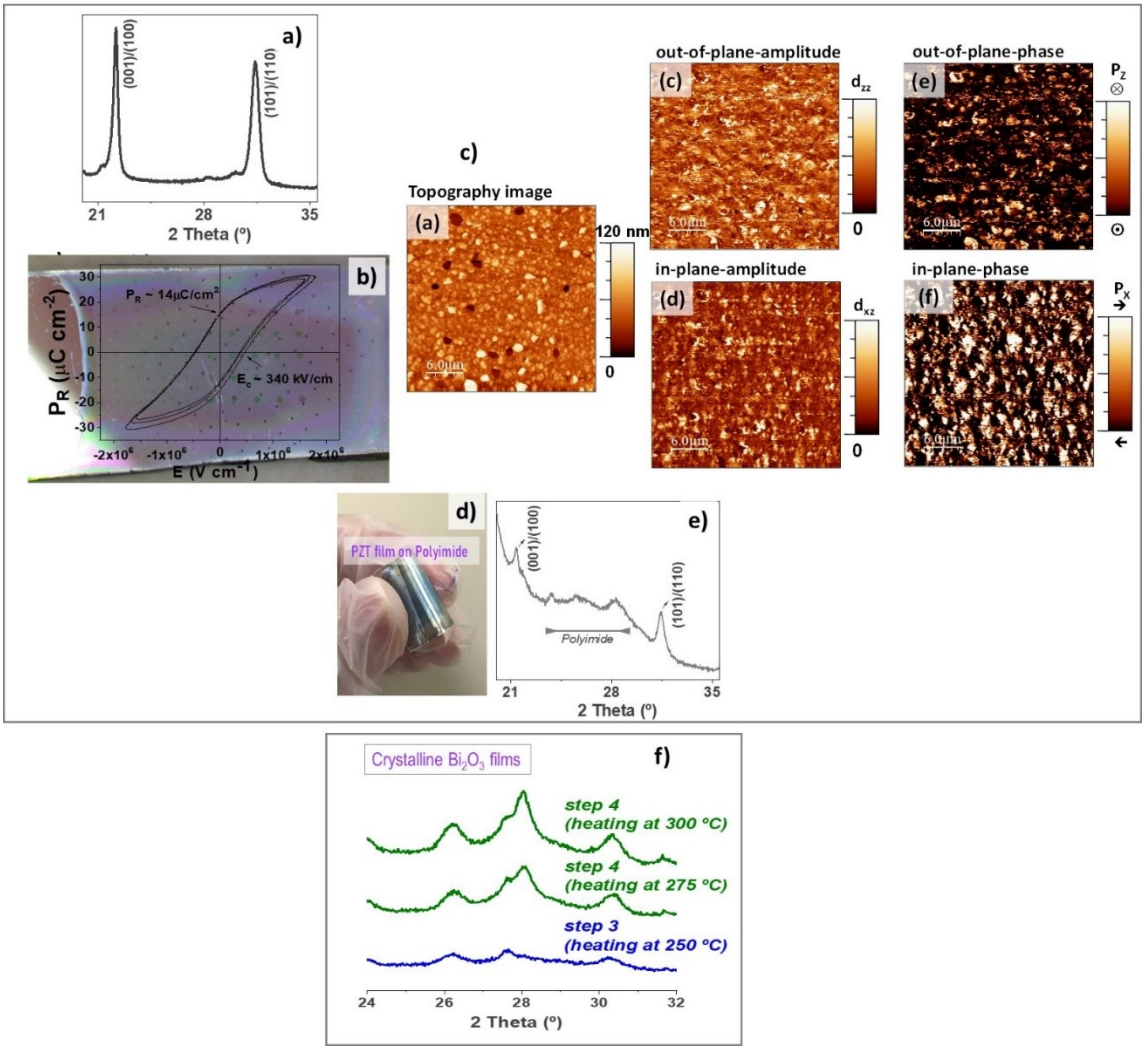

Figure S9. Validation of the general application of the solution deposition method developed here for the fabrication of crystalline thin films of any metal oxide directly on temperature-sensitive substrates, which is a key requirement for the next-generation high-performance and flexible devices demanded today by the emerging. a) X-ray diffraction pattern of a $Pb(Zr_{0.30}Ti_{0.70})O_3$ (PZT) thin film on a Pt-coated (100) Si substrate that has been obtained at 350ºC with the preparation process devised in this work. b) Photograph of the array of capacitors fabricated for the electrical characterization at the macroscale of the former film. Representative ferroelectric hysteresis loops measured in this film are inserted in this figure. c) AFM topography image of the former film and its ferroelectric characterization measured at the nanoscale by PFM. d) Photograph of a PZT film directly prepared on flexible polyimide substrates. e) X-ray diffraction pattern of this flexible PZT film. The X-ray reflections of the PZT films have been indexed according with the JCPDS-ICDD card No. 01-070-4055 of the $Pb(Zr_{0.30}Ti_{0.70})O_3$ perovskite. f) X-ray diffraction patterns of crystalline Bi_2O_3 thin films obtained after the steps 3 and 4 of the process. Reflections corresponding to the Bi_2O_3 crystalline oxide are observed just after the step 3, where the sample is heated at only 250ºC during the UV-irradiation process. The increasing of the annealing temperature during the step 4 produces a better crystallization of the films, observed by the higher intensity of the Bi_2O_3 reflections.

References

[1] J. T. Anderson, C .L .Munsee, C. M. Hung, T. M. Phung, G. S. Herman, D. C. Johnson, J. F. Wager, D. A. Keszler., *Adv.Funct.Mater*., **2007**, *17*, 2117.

[2] S. T. Meyers, J. T. Anderson, D. Hong, C. M. Hung, J. F. Wager, D. A. Keszler, *Chem. Mater*., **2007**, *19*, 4023.

[3] K. M. Kim, C. W. Kim, J.-S. Heo, H. Na, J. E. Lee, C. B. Park, J.-U. Bae, C.-D. Kim, M. Jun, Y. K. Hwang, S. T. Meyers, A. Grenville, D. A. Keszler., *Appl. Phys. Lett*., **2011,** *99*, 242109.

[4] J.-B. Seon, S. Lee, J. M. Kim, H.-D. Jeong., *Chem. Mater*., **2009**, *21*, 604.

[5] K. Jiang, J. T. Anderson, K. Hoshino, D. Li, J. F. Wager, D. A. Keszler. *Chem. Mater.*, **2011**, *23*, 945.

[6] J. H. Park, S. J. Lee, T. I. Lee, J. H. Kim, C. H. Kim, G. S. Cha, M. H. Ham, H. K. Baik, J. M .Myoung. *J. Mater. Chem. C*, **2013**, *1*, 1840.

[7] W. Yang, K. Song, Y. Jung, S. Jeong, J. Moon***. J. Mater. Chem. C*,* 2013**, *1*, 4275.

[8] J. H. Park, K. Kim, Y. B. Yoo, S. Y. Park, K.-H. Lim, K. H. Lee, H. K. Baik, Y. S.Kim. *J. Mater. Chem. C*, **2013**, *1*, 7166.

[9] J. H. Park, Y. B. Yoo, K. H. Lee, W. S. Jang, J. Y. Oh, S. S. Chae, H. K. Baik. *ACS Appl. Mater. Interfaces*, **2012**, *5*, 410.

[10] J. H. Park, S. J. Lee, T. I. Lee, J. H. Kim, C.-H. Kim, G. S. Chae, M.-H. Ham, H. K.Baik, J.-M. Myoung. *J. Mater. Chem. C*, **2013**, *1*, 1840.

[11] K. Jiang, S. T. Meyers, M. D. Anderson, D. C. Johnson, D. A. Keszler. *Chem. Mater.*, **2012**, *25*, 210.

[12] S. Choi, B.-Y. Park, H.-K. Jung. *Thin Solid Films*, **2013**, *534*, 291.

[13] Y. S. Rim, H. Chen, X. Kou, H.-S. Duan, H. Zhou, M. Cai, H. J. Kim, Y. Yang. *Adv. Mater*., **2014**, *26(25)*, 4273.

[14] W. Xu, H. Wang, F. Xie, J. Chen, H. Cao, J. -B. Xu. *ACS Appl. Mater. Interfaces*, **2015**, *7*, 5803.

[15] J. Chung, Y. J. Tak, W.G.Kim, J. W. Park, T. S. Kim, J. H. Lim, H. J. Kim. *J. Mater. Chem. C*, **2018**, *6*, 4928.

[16] J. Kim, M. Kim, Y. Kang, K. –T. Kim, J. –S. Heo, S. K. Park, Y. –H. Kim. *Journal of Alloys and Compounds*, **2020**, *842*, 155671.

[17] M. Mandeljc, M. Kosec, B. Maliˇc, and Z. Samardzija. *Integr. Ferroelectr*., **2000,** *30(1–4)*, 149.

[18] M. Kosec, B. Malic, and M. Mandeljc. *Mater. Sci. Semicond. Process*., **2002**, *5(2–3)*, 97.

[19] M. Calzada, I. Bretos, R. Jimenez, H. Guillon, L. Pardo. *Adv.Mater*., **2004**, *16(18)*, 1620.

[20] N. Martín-Arbella, I. Bretos, R. Jiménez, M. L. Calzada, R. Sirera. *J. Amer. Ceram. Soc.*, **2011**, *94(2)*, 396.

[21] D. Pérez-Mezcua, R. Sirera, R. Jimenez, I. Bretos, C. De Dobbelaere, A. Hardy, M. K. Van Bael, M. L. Calzada. *J. Mater. Chem.* ***C*****,* 2014**, *2(41)*, 8750.

[22] I. Bretos, R. Jiménez, A. Wu, A. I. Kingon, P. M. Vilarinho, M. L. Calzada. *Adv. Mater.*, **2014**, *26(9)*, 1405.

[23] E. K. Michael-Sapia, H. U. Li, T. N. Jackson, S. Trolier-McKinstry. *J. Appl. Phys*., **2015**, *118(23)*, 234102.

[24] M. Tomczyk, I. Bretos, R. Jimenez, A. Mahajan, E. V. Ramana, M. L. Calzada, P. M. Vilarinho. *J. Mater. Chem. C*, **2017**, *5(47)*, 12529.

[25] I. Bretos, R. Jiménez, D. Pérez-Mezcua, N. Salazar, J. Ricote, M. L. Calzada. *Adv. Mater*., **2015**, *27(16)*, 2608.

[26] I. Bretos, R. Jimenez, J. Ricote, R. Sirera, M. L. Calzada. *Adv.Funct.Mater*., **2020**, *30(32)*, 2001897.
[27] O. Barrios, R. Jiménez, J. Ricote, P. Tartaj, M. L. Calzada, I. Bretos. *Adv. Funct. Mater.*, **2022**, *32(27)*, 2112944.
[28] P. T. Tue, T. Shimoda, Y. Takamura. *Appl.Phys.Letts*., **2020**, *8*, 021112.
[29] N. Martín-Arbella, I. Bretos, R. Jiménez, M. L. Calzada, R. Sirera. *J. Amer. Ceram. Soc.*, **2011**, *94(2)*, 396.
[30] D. Pérez-Mezcua, R. Sirera, R. Jimenez, I. Bretos, C. De Dobbelaere, A. Hardy, M. K. Van Bael, M. L. Calzada. *J. Mater. Chem. C*, **2014**, *2(41)*, 8750.
[31] A. Gómez-López. "Flexible ferroelectric $BiFeO_3$ perovskite thin films processed by photo-chemical solution deposition". MSc, Facultad de Ciencias. Universidad Autónoma de Madrid, Spain. June **2021.**
[32] C. Yang, C. Wöll, Advances in Physics: X, **2017**, 2:2, 373-408, DOI:10.1080/23746149.2017.1296372
[33] Born, Max; Wolf, Emil (1980). "Principles of optics: electromagnetic theory of propagation, interference and diffraction of light". Oxford; New York: Pergamon Press. 6th ed., ISBN 0-08-026482-4. OCLC 7106160
[34] Max Born, Kun Huang, "Dynamical Theory of Crystal Lattices". Clarendon Press, **1988**, ISBN 0198503695, 9780198503699
[35] Y.-H. Kim, J.-S. Heo, T.-H. Kim, S. Park, M.-H. Yoon, J. Kim, M. S. Oh, G.-R. Yi, Y.-Y. Noh, S. K. Park. *Nature*, **2012**, *489*, 128.
[36] J.C. Dupin, D. Gonbeau, P. Vinatier, A. Levasseur. *Phys.Chem.Chem.Physics*, **2000**, *2(6)*, 1319.
[37] A. L. Kholkin, S. O. Iakovlev, J. L. Baptista. Direct effect of illumination on ferroelectric properties of lead zirconate titanate thin films. *Appl. Phys. Lett.*, **2001**, *79*, 2055-2057.
[38] Y. J. Tak, D. H. Yoon, S. Yoon, U. H. Choi, M. M. Sabri, B. D. Ahn, H. J. Kim. Enhanced Electrical Characteristics and Stability via Simultaneous Ultraviolet and Thermal Treatment of Passivated Amorphous In-Ga-Zn-O Thin-Film Transistors. *ACS Appl. Mater. Interf*., **2014**, *6(9)*, 6399-6405.
[39] H. Shineiki, M. Nakata, M. UV-O_3 and dry-O_2-2-step annealed chemical vapor-deposited Ta_2O_5 films for storage dielectrics of 64-MB DRAMS. *IEEE Transact. Electr. Dev*., **1991**, *38(3)*, 455.